

Reservoir Predictive Path Integral Control for Unknown Nonlinear Dynamics

Daisuke Inoue, Tadayoshi Matsumori, Gouhei Tanaka, *Member, IEEE*, and Yuji Ito, *Senior Member, IEEE*

Abstract—Neural networks capable of approximating complex nonlinearities have found extensive application in data-driven control of nonlinear dynamical systems. However, fast online identification and control of unknown dynamics remain central challenges. This paper integrates echo-state networks (ESNs)—reservoir computing models implemented with recurrent neural networks—and model predictive path integral (MPPI) control—sampling-based variants of model predictive control—to meet these challenges. The proposed reservoir predictive path integral (RPPI) enables fast learning of nonlinear dynamics with ESN and exploits the learned nonlinearities directly in parallelized MPPI control computation without linearization approximations. The framework is further extended to uncertainty-aware RPPI (URPPI), which leverages ESN uncertainty to balance exploration and exploitation: exploratory inputs dominate during early learning, while exploitative inputs prevail as model confidence grows. Experiments on controlling the Duffing oscillator and four-tank systems demonstrate that URPPI improves control performance, reducing control costs by up to 60% compared to traditional quadratic programming-based model predictive control methods.

Index Terms—Reservoir Computing, Echo State Network, Model Predictive Control, Path Integral Control, Nonlinear Control, Online Learning

I. INTRODUCTION

ACHIEVING high-precision, real-time control of systems with unknown dynamics is challenging in many industrial applications. Standard approaches first estimate the system model through identification, then design model-based control [1], [2]. When the target system is linear, this approach can achieve high control performance based on mature identification and control theory. However, real-world systems exhibit nonlinearities, making linear theory inadequate and degrading performance [3]. To address this, machine learning-based modeling integrated with model-based control has gained much attention [4]–[8]. Neural networks (NNs) [4]–[8] and Gaussian process regression (GPR) [9], [10] with nonlinear model predictive control (MPC) show promise for nonlinear systems. NNs deliver accurate identification of nonlinear dynamics, whereas GPR enables uncertainty-aware control. This study focuses on integrating data-driven models with MPC to enable real-time control of unknown nonlinear systems.

Although combining machine learning models with nonlinear MPC has shown great promise for controlling nonlinear systems, such approaches often encounter computational challenges in real-time applications. NN-based approaches incur excessive computational overhead in learning model parameters and nonlinear optimization in nonlinear MPC [11]. Similarly, GPR-based methods suffer from computational complexity that scales cubically with the number of training samples [12], [13]. One approach to address these computational challenges is explicit MPC, which pre-computes optimal input mappings [14], [15]. However, required storage and computation demands become prohibitive as the dimensions of the control system’s input and output spaces increase [16]. Consequently, the development of methods that achieve both fast online identification and control remains a fundamental challenge in nonlinear control [15], [17], [18].

Reservoir computing, a framework for efficient neural computation, offers fast training and strong temporal modeling capabilities; among its variants, echo state networks (ESNs) are particularly notable for their simplicity and rapid adaptation [19]–[21]. Unlike conventional recurrent NNs, ESNs offer computational efficiency in online training, since only output weights need to be optimized [22]. Using recursive least squares (RLS), the output weights are updated in a computationally efficient manner. Among nonlinear MPC approaches combined with ESN, quadratic programming MPC (QPMPC) has gained attention because of its computational efficiency and real-time capability [23]–[26]. This method linearizes a plant model at each control step, casting the optimization problem as a quadratic programming (QP) problem and enabling rapid computation of the optimal control inputs. This approach facilitates online computation of control inputs for nonlinear systems in a computationally efficient manner.

ESN-based QPMPC approaches exhibit two limitations. First, linearizing ESN models and restricting a cost function to a quadratic form both limit the method’s applicability. Because the ESN is linearized at every control step, its nonlinear expressive power cannot be fully exploited, leading to large prediction errors when the plant exhibits strong nonlinearity. Furthermore, constraining the cost function to a quadratic form prevents the inclusion of higher-order terms required by certain control objectives. Thus, developing online control methods that address these limitations remains a pressing research challenge. Second, earlier studies [23]–[26] do not discuss the exploration-exploitation trade-off in simultaneous online identification and control. Control inputs that span a wide range of frequencies usually improve identification accuracy,

Corresponding authors: Daisuke Inoue, Yuji Ito

This study is partly supported by JSPS KAKENHI Grant Numbers JP23K28154, JP25H00451, JST Moonshot R&D Grant Number JPMJMS2021, and JST CREST Grant Number JPMJCR24R2.

D. Inoue, T. Matsumori, and Y. Ito are with Toyota Central R&D Labs., Inc., Nagakute, Aichi 480-1192, Japan

G. Tanaka is with Nagoya Institute of Technology, Nagoya, Aichi, 466-8555, Japan

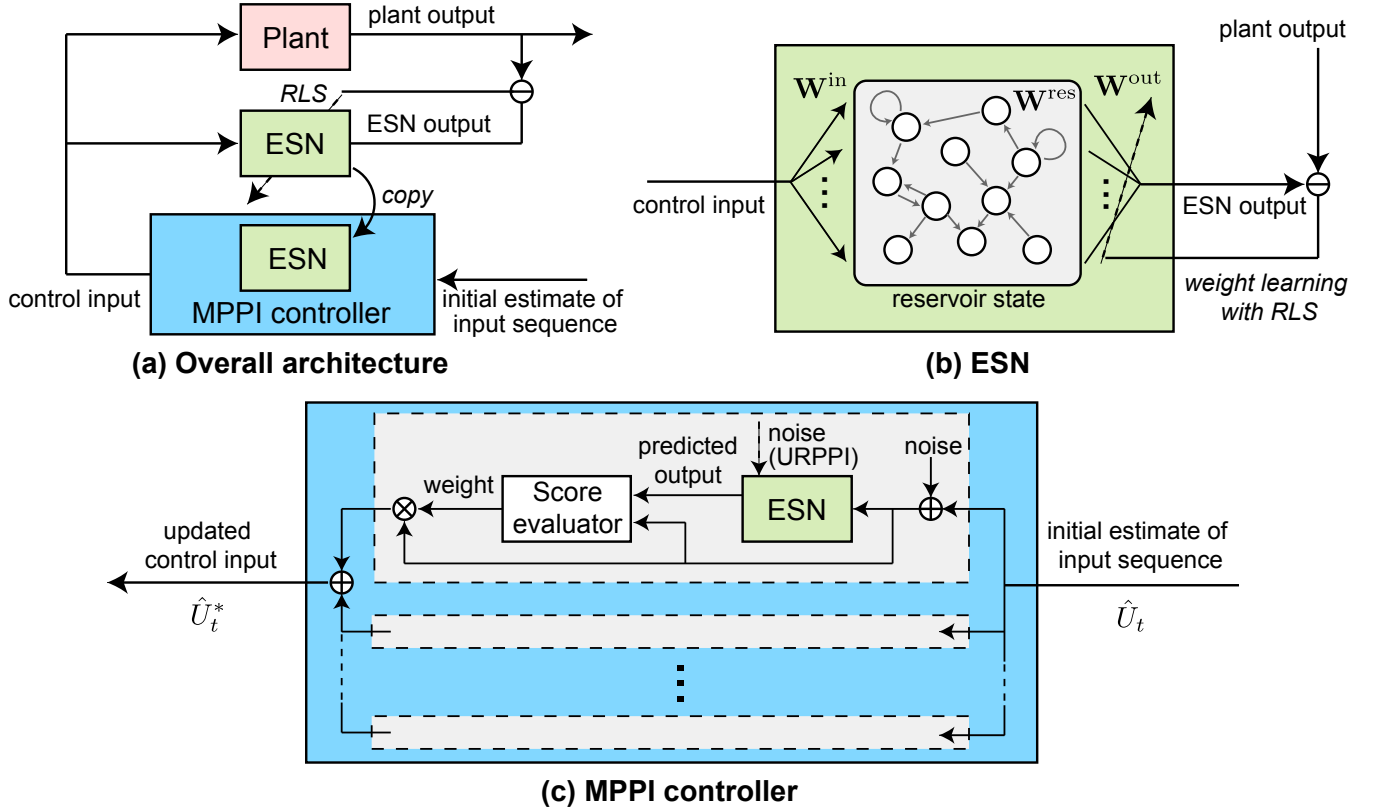


Fig. 1: Schematic diagram of the proposed RPPI that integrates ESN and MPPI. (a) Overall architecture of RPPI; (b) ESN model for online identification of nonlinear dynamics, in which only the output weight matrix is trained with RLS; (c) MPPI controller for computing control inputs based on the learned ESN models. In URPPPI, the output is predicted using the perturbed output weight matrices so that the controller can compute control inputs that balance exploration and exploitation.

but they can reduce tracking performance, clearly showing this conflict [1]. Thus, practical control methods that automatically balance these two goals in real time constitute a key challenge.

To solve the above challenges, we propose an online control method for nonlinear systems, called *reservoir predictive path integral (RPPI)*, which combines an ESN with model predictive path integral (MPPI) control [27]. MPPI is a sampling-based control method that generates numerous input trajectories and computes their weighted average to determine the control input. This approach directly treats nonlinear dynamics and arbitrary cost functions without requiring explicit optimization solvers [28]. Real-time computation has also been shown to be possible through parallel sampling using GPUs [29]. Furthermore, we propose *uncertainty-aware RPPI (URPPPI)*, which incorporates model uncertainty into MPPI input weighting. The model uncertainty is quantified through the precision matrix of the ESN output weight matrix, which is estimated via RLS. This mechanism autonomously balances exploration and exploitation by initially selecting exploratory inputs before model identification converges and later shifting toward exploitative inputs as model confidence increases. The main contributions of this research are summarized as follows:

- **Online MPC for unknown nonlinear dynamics:** We propose an RPPI control framework that enables online MPC for strongly nonlinear unknown systems and arbitrary cost functions *without* linearization.

- **Uncertainty-guided control input:** We extend RPPI to a URPPPI by injecting the ESN output-weight covariance into the MPPI weighting mechanism, which enables automatic scheduling between exploratory and exploitative control inputs.
- **Experimental validation:** We demonstrate the effectiveness of the proposed approach on the Duffing oscillator and four-tank system benchmarks, where URPPPI achieves up to 60% lower control cost than ESN-based QPMPC.

The schematic diagram of the proposed method is shown in Fig. 1.

In the following, Section II reviews related work on ESN-based MPC and machine learning approaches to control. Section III presents the problem setting of this research. Next, Section IV introduces the ESN model and its learning algorithm, RLS, and then proposes RPPI and URPPPI as methods that integrate ESN with MPPI. In Section V, we conduct numerical simulations to evaluate the performance of the proposed methods. Finally, conclusions and directions for future work are discussed in Section VI.

Notation. For a matrix $A \in \mathbb{R}^{m \times n}$, the vectorization $\text{vec}(A)$ is defined as $\text{vec}(A) := [a_{11}, \dots, a_{m1}, \dots, a_{1n}, \dots, a_{mn}]^T \in \mathbb{R}^{mn}$, where a_{ij} denotes the (i, j) -th entry of A . For matrices $A \in \mathbb{R}^{m \times n}$ and $B \in \mathbb{R}^{p \times q}$, the Kronecker product $A \otimes B \in$

$\mathbb{R}^{mp \times nq}$ is defined as

$$A \otimes B := \begin{bmatrix} a_{11}B & \cdots & a_{1n}B \\ \vdots & \ddots & \vdots \\ a_{m1}B & \cdots & a_{mn}B \end{bmatrix}.$$

For a random variable v with density p_v , the expectation of a function f is denoted by $\mathbb{E}_{p_v}[f(v)]$. The symbol $\mathcal{N}(\mu, \Sigma)$ denotes the multivariate normal distribution with mean μ and covariance matrix Σ , and its density function is written as $\mathcal{N}(\cdot|\mu, \Sigma)$.

II. RELATED WORK

Several ESN-based MPC approaches have been proposed, each with distinct characteristics and limitations. Pan and Wang [23] introduced ESNs as surrogate models for nonlinear MPC by training the ESN offline and applying a first-order Taylor expansion to convexify the optimization into QP; because the model is fixed and locally linearized, the controller struggles with strong nonlinear dynamics and cannot adapt to new data. Jordanou *et al.* [24] preserved part of the ESN's nonlinearity by separating forced and free responses, yet they still linearize and solve a QP at every step. Schwedersky *et al.* [25] added RLS updates so that the ESN adapts online, but their controller linearizes the ESN and solves a QP each iteration. In contrast, the proposed *RPPI/URPPI* framework eliminates *all* linearization approximations through sampling-based path-integral control.

Learning-based control methods face a trade-off between model expressiveness and computational efficiency. NN models, including recurrent NN (RNN), gated recurrent units (GRU), long short-term memory (LSTM), transformer model, input convex NN (ICNN), and graph NN (GNN), offer high expressiveness but require computationally expensive gradient computations for online learning [4]–[8], [30]–[32]. GPR-based approaches provide uncertainty quantification but suffer from $O(N_{\text{data}}^3)$ computational complexity, where N_{data} is the number of training data points, limiting real-time applicability [9], [10]. The ESN architecture balances nonlinear modeling capability with computational efficiency by fixing the input and internal reservoir weights and adapting only the linear readout weights through $O(\hat{N}^2)$ RLS recursions, where \hat{N} is the reservoir state dimension.

Our control strategy is based on MPPI, a sampling-based framework that enables efficient computation of control inputs for complex and non-differentiable dynamics [27]. We extend this foundation to incorporate model uncertainty. While other uncertainty-aware approaches exist, such as tube-based or risk-aware MPPI [33], [34], our approach utilizes a computationally efficient mechanism. Specifically, we use the covariance matrix of the ESN's output weights, obtained as a natural byproduct of the RLS learning process, as a measure of parametric uncertainty. As a result, the controller can dynamically adjust the balance between exploration and exploitation.

III. PROBLEM FORMULATION

In this paper, we consider a control system with input dimension $M \in \mathbb{N}$, state dimension $N \in \mathbb{N}$, and output dimension $L \in \mathbb{N}$, described as follows:

$$\mathbf{z}_{t+1} = \mathbf{F}(\mathbf{z}_t, \mathbf{u}_t), \quad (1)$$

$$\mathbf{y}_t = \mathbf{G}(\mathbf{z}_t), \quad (2)$$

where $\mathbf{z}_t \in \mathbb{R}^N$ is the state vector, $\mathbf{u}_t \in \mathbb{R}^M$ is the input vector, and $\mathbf{y}_t \in \mathbb{R}^L$ is the output vector. The symbol $\mathbf{F}: \mathbb{R}^N \times \mathbb{R}^M \rightarrow \mathbb{R}^N$ and $\mathbf{G}: \mathbb{R}^N \rightarrow \mathbb{R}^L$ are the state transition function and output function, respectively.

For such a control system, we consider the problem of finding a control input that minimizes the following cost function J_{ctrl} at each time t :

$$\underset{U_t \in \mathcal{U}}{\text{minimize}} J_{\text{ctrl}}(U_t), \quad (3)$$

$$J_{\text{ctrl}}(U_t) := C(\mathbf{y}_t, \mathbf{y}_{t+1}, \dots, \mathbf{y}_{t+H}) + \sum_{\tau=t}^{t+H-1} \frac{1}{2} (\mathbf{u}_\tau - \mathbf{u}^{\text{ref}})^\top R (\mathbf{u}_\tau - \mathbf{u}^{\text{ref}}), \quad (4)$$

where $\mathcal{U} \subseteq \mathbb{R}^{M \times H}$ is the set of admissible control inputs, and $H \in \mathbb{N}$ is a positive constant representing the prediction horizon. Additionally, $R \in \mathbb{R}^{M \times M}$ is a positive definite matrix representing input weights, and $\mathbf{u}^{\text{ref}} \in \mathbb{R}^M$ is a vector representing the reference value for the control input. The function C is a cost function related to the time series of the output vectors, expressed using output cost functions $\ell: \mathbb{R}^L \rightarrow \mathbb{R}$ and $\phi: \mathbb{R}^L \rightarrow \mathbb{R}$ as follows:

$$C(\mathbf{y}_t, \mathbf{y}_{t+1}, \dots, \mathbf{y}_{t+H}) := \sum_{\tau=t}^{t+H-1} \ell(\mathbf{y}_\tau) + \phi(\mathbf{y}_{t+H}). \quad (5)$$

In this paper, we assume that the state vector \mathbf{z}_t and its dimension N , state transition function \mathbf{F} , and output function \mathbf{G} in (2) are unknown, and only the output data \mathbf{y}_t when input data \mathbf{u}_t is applied is observed. The goal of this paper is to find a control input U_t that minimizes the above cost function while identifying the dynamics of (1) and (2).

IV. PROPOSED METHOD

This section presents the proposed framework that integrates ESN with MPPI and uncertainty-aware MPPI (UMPPI), addressing computational and performance limitations in existing approaches. The framework combines ESN's rapid parameter adaptation capabilities with MPPI's sampling-based optimization to enable online control of unknown nonlinear systems without linearization approximations. The proposed methods, RPPI and URPPI, operate through the following three-step cycle at each control iteration:

- 1) Update the ESN output weight matrix $\mathbf{W}_t^{\text{out}}$ and its precision matrix \mathbf{P}_t using RLS.
- 2) Compute the control input sequence \hat{U}_t^* using MPPI or UMPPI, where UMPPI extends MPPI by injecting ESN output weight uncertainty into the sampling process.
- 3) Update the reservoir state \mathbf{x}_t and control system state \mathbf{z}_t by applying input $\hat{\mathbf{u}}_t^*$, the first component of \hat{U}_t^* .

Algorithm 1: RPPI/URPPI

Given: Initial reservoir state \mathbf{x}_0 , initial estimate of input sequence \hat{U}_{-1} , terminal time T , initial output weight $\mathbf{W}_{-1}^{\text{out}}$ and precision matrix \mathbf{P}_{-1} .

$t \leftarrow 0$.

while $t < T$ **do**

Update the ESN output weight $\mathbf{W}_t^{\text{out}}$ and the precision matrix \mathbf{P}_t using RLS (Algorithm 2) with the observed plant output \mathbf{y}_t , reservoir state \mathbf{x}_t , previous output weight $\mathbf{W}_{t-1}^{\text{out}}$, and precision matrix \mathbf{P}_{t-1} .

Calculate the control input sequence \hat{U}_t^* with MPPI/UMPPI (Algorithm 3), using previous sequence $\hat{U}_t = \hat{U}_{t-1}^*$, reservoir state \mathbf{x}_t , output weight $\mathbf{W}_t^{\text{out}}$ and precision matrix \mathbf{P}_t .

Apply the first component \hat{u}_t^* of \hat{U}_t^* to both the ESN and plant to update each state \mathbf{x}_{t+1} and \mathbf{z}_{t+1} .

$t \leftarrow t + 1$.

end

An overview of the proposed method is shown in Algorithm 1. The remainder of this section details the components of the proposed framework. Section IV-A describes the ESN architecture and online learning using RLS. Section IV-B explains the MPPI-based control input computation using the ESN model. Section IV-C evaluates the computational complexity of the overall procedure.

A. Echo State Network

We describe the ESN model and its learning method. We employ the ESN with leaky terms, which explicitly incorporates temporal dynamics through leak rates of the target control system [20]. For the learning method, we employ online learning via RLS [35].

1) *Model:* The input-output relationship in (1) and (2) is modeled using the following ESN [20]:

$$\mathbf{x}_{t+1} = (1 - \alpha)\mathbf{x}_t + \alpha f(\mathbf{W}^{\text{res}}\mathbf{x}_t + \mathbf{W}^{\text{in}}\mathbf{u}_t), \quad (6)$$

$$\hat{\mathbf{y}}_t = \mathbf{W}_t^{\text{out}\top}\mathbf{x}_t. \quad (7)$$

Here, $\mathbf{x}_t \in \mathbb{R}^{\hat{N}}$ is the reservoir state vector, where $\hat{N} \in \mathbb{N}$, and $\hat{\mathbf{y}}_t \in \mathbb{R}^L$ is the output vector. Additionally, $\mathbf{W}^{\text{res}} \in \mathbb{R}^{\hat{N} \times \hat{N}}$ and $\mathbf{W}^{\text{in}} \in \mathbb{R}^{\hat{N} \times M}$ are the state and input weight matrices, respectively, and $\mathbf{W}_t^{\text{out}} \in \mathbb{R}^{\hat{N} \times L}$ is the output weight matrix. Furthermore, $f: \mathbb{R}^{\hat{N}} \rightarrow \mathbb{R}^{\hat{N}}$ is an element-wise nonlinear activation function called the activation function, and $\alpha \in (0, 1]$ is a parameter called the leak rate.

In contrast to conventional NNs, the state and input weight matrices \mathbf{W}^{res} and \mathbf{W}^{in} remain fixed as randomly initialized matrices. In many cases, the reservoir state dimension \hat{N} is set greater than the input or output dimensions. The matrix \mathbf{W}^{res} is a sparse random matrix with many components equal to zero, designed empirically so that the maximum absolute value of eigenvalues (spectral radius) is 1 or less. The matrix \mathbf{W}^{in} is randomly generated from a uniform distribution. The reservoir

Algorithm 2: RLS [35]

Given: Discount factor γ , previous output weight $\mathbf{W}_{t-1}^{\text{out}}$, precision matrix \mathbf{P}_{t-1} , observed output \mathbf{y}_t , and current state \mathbf{x}_t .

$\mathbf{W}_t^{\text{out}} \leftarrow \mathbf{W}_{t-1}^{\text{out}} + \frac{\mathbf{P}_{t-1}\mathbf{x}_t}{\gamma + \mathbf{x}_t^\top \mathbf{P}_{t-1}\mathbf{x}_t} (\mathbf{y}_t - \mathbf{W}_{t-1}^{\text{out}\top}\mathbf{x}_t)^\top$.

$\mathbf{P}_t \leftarrow \frac{1}{\gamma} \left(\mathbf{P}_{t-1} - \frac{\mathbf{P}_{t-1}\mathbf{x}_t\mathbf{x}_t^\top \mathbf{P}_{t-1}}{\gamma + \mathbf{x}_t^\top \mathbf{P}_{t-1}\mathbf{x}_t} \right)$.

return $\mathbf{W}_t^{\text{out}}$ and \mathbf{P}_t

state dimension \hat{N} , sparseness and spectral radius of \mathbf{W}^{res} , the shape of the activation function f , the leak rate α , and the range of the input weight matrix \mathbf{W}^{in} are hyperparameters that must be set prior to learning.

2) *Learning Algorithm:* We describe the learning method for the output weight matrix \mathbf{W}^{out} , which is the only learnable parameter in ESN [35]. This weight matrix is learned to minimize the error between the observed output and the model output, written as follows:

$$J_{\text{id}}(\mathbf{W}^{\text{out}}) = \sum_{\tau=0}^t \gamma^{t-\tau} \|\mathbf{y}_\tau - \mathbf{W}^{\text{out}\top}\mathbf{x}_\tau\|_2^2, \quad (8)$$

where $\gamma \in (0, 1]$ is the discount factor.

Proposition IV.1 (Ref. [35]). Assume that for every time $t \geq \hat{N} - 1$, the matrix $\mathbf{A}_t := \sum_{\tau=0}^t \gamma^{t-\tau} \mathbf{x}_\tau \mathbf{x}_\tau^\top$ is invertible. Then, the minimizer $\mathbf{W}_t^{\text{out}*}$ at time $t \geq \hat{N}$ can be expressed using the minimizer $\mathbf{W}_{t-1}^{\text{out}*}$ at time $t - 1$ as follows:

$$\mathbf{W}_t^{\text{out}*} = \mathbf{W}_{t-1}^{\text{out}*} + \frac{\mathbf{P}_{t-1}\mathbf{x}_t}{\gamma + \mathbf{x}_t^\top \mathbf{P}_{t-1}\mathbf{x}_t} (\mathbf{y}_t - \mathbf{W}_{t-1}^{\text{out}*}\mathbf{x}_t)^\top, \quad (9)$$

$$\mathbf{P}_t = \frac{1}{\gamma} \left(\mathbf{P}_{t-1} - \frac{\mathbf{P}_{t-1}\mathbf{x}_t\mathbf{x}_t^\top \mathbf{P}_{t-1}}{\gamma + \mathbf{x}_t^\top \mathbf{P}_{t-1}\mathbf{x}_t} \right), \quad (10)$$

where $\mathbf{P}_t = \mathbf{A}_t^{-1} \in \mathbb{R}^{\hat{N} \times \hat{N}}$ is called the precision matrix of the variable \mathbf{x}_t .

The sequential learning method that repeatedly applies (9) and (10) with arbitrarily initialized parameters $\mathbf{W}_{-1}^{\text{out}}$ and \mathbf{P}_{-1} is called RLS [35]. The RLS algorithm for ESN is shown in Algorithm 2.

The following proposition states that the precision matrix \mathbf{P}_t of the variable \mathbf{x}_t represents the covariance of the estimated output weight matrix $\mathbf{W}_t^{\text{out}}$. This result is obtained by extending the analysis in Ref. [35] to the case of ESNs, where the estimated parameters take a matrix form.

Proposition IV.2. Assume that there exists a weight $\bar{\mathbf{W}}^{\text{out}} \in \mathbb{R}^{\hat{N} \times L}$ such that at any time t , the relationship between the reservoir state and the true plant output is expressed as

$$\mathbf{y}_t = \bar{\mathbf{W}}^{\text{out}\top}\mathbf{x}_t + \boldsymbol{\epsilon}_t, \quad (11)$$

where $\boldsymbol{\epsilon}_t \in \mathbb{R}^L$ is noise that follows a normal distribution with mean 0 and covariance matrix $\tilde{\Sigma} = \text{diag}(\sigma_1^2, \dots, \sigma_L^2)$ independently at each time. Then, if $\gamma = 1$,

$$\mathbb{E}[\text{vec}(\mathbf{W}_t^{\text{out}*} - \bar{\mathbf{W}}^{\text{out}})\text{vec}(\mathbf{W}_t^{\text{out}*} - \bar{\mathbf{W}}^{\text{out}})^\top] = \tilde{\Sigma} \otimes \mathbf{P}_t. \quad (12)$$

This property is used when adding perturbations to the output weight matrix in UMPPI, as described in Section IV-B.

B. Uncertainty-aware Model Predictive Path Integral Control

We propose control methods combining the ESN with MPPI or its uncertainty-aware variant UMPPI. In MPPI, multiple noisy input sequences are sampled based on a reference input to simulate future trajectories of the control system, and an output cost is computed for each sequence [27]. The optimal control input is approximately computed as a weighted average of many samples, where samples with lower costs receive higher weights. In UMPPI, in addition to sampling input sequences, output weight matrices of the ESN with noise added are sampled. The magnitude of the noise applied to the output matrices is determined by the precision matrix \mathbf{P}_t in RLS. This provides control input perturbations according to the identification accuracy, resulting in automatic adjustment of exploration and exploitation. Note that in Algorithm 3 described later below, when the sample size $\tilde{K} = 1$ and the noise covariance $\tilde{\Sigma} = 0$, UMPPI reduces to the standard MPPI algorithm. Therefore, we focus on the UMPPI formulation in the following description.

Remark IV.3. The following derivation of UMPPI extends the framework of Ref. [27] by introducing perturbations of the output-weight matrix. This extension preserves the mathematical consistency of the MPPI formulation and constitutes a main contribution of the present work. Specifically, Proposition IV.4 parallels Eq. (13) in Ref. [27]; Proposition IV.5 is established by the same argument as in Section III-A of that reference; and Proposition IV.6 corresponds to Eq. (27) in the same reference.

To explain the theoretical foundation of the proposed control algorithm, we outline how UMPPI computes the optimal control solution through a sequence of sampling-based approximations. The derivation of UMPPI proceeds in the following three steps:

- 1) **Stochastic reformulation.** The original MPC problem is first recast as a stochastic optimization over noise-injected input sequences, as expressed in (20).
- 2) **Free-energy relaxation.** Introducing a free-energy functional converts this stochastic problem into the minimization of a Kullback–Leibler divergence between two probability distributions (see (31)).
- 3) **Sampling-based optimization.** The resulting optimal input sequence is then approximated by Monte Carlo integration with importance sampling, as implemented in Algorithm 3.

This formulation offers a sampling-based interpretation of MPC, where control sequences are drawn from a distribution and weighted according to their associated costs. The details of each step are described in Sections IV-B1 to IV-B3.

1) *Stochastic reformulation:* This subsection reformulates the original MPC problem in (3) as a stochastic optimization problem over perturbed control inputs and model parameters in (20). Like conventional MPPI, UMPPI considers perturbed inputs $\mathbf{v}_t \sim \mathcal{N}(\mathbf{u}_t, \Sigma)$ where noise is applied to some initial inputs \mathbf{u}_t as follows:

$$\hat{\mathbf{x}}_{\tau+1} = \hat{\mathbf{F}}(\hat{\mathbf{x}}_\tau, \mathbf{v}_\tau), \quad \hat{\mathbf{x}}_t = \mathbf{x}_t. \quad (13)$$

Here, $\hat{\mathbf{F}}: \mathbb{R}^{\hat{N}} \times \mathbb{R}^M \rightarrow \mathbb{R}^{\hat{N}}$ represents the state update equation in (6):

$$\hat{\mathbf{F}}(\hat{\mathbf{x}}_\tau, \mathbf{v}_\tau) := (1 - \alpha)\hat{\mathbf{x}}_\tau + \alpha f(\mathbf{W}^{\text{res}}\hat{\mathbf{x}}_\tau + \mathbf{W}^{\text{in}}\mathbf{v}_\tau). \quad (14)$$

Furthermore, $\Sigma \in \mathbb{R}^{M \times M}$ represents the covariance matrix of the applied noise, and its value is determined based on the input weight matrix R of the cost function (3) as follows:

$$\Sigma = \lambda R^{-1}, \quad (15)$$

where $\lambda \in \mathbb{R}$ is a parameter called the inverse temperature, which is a design parameter. In addition to this, UMPPI considers outputs using weight matrices \mathbf{W}_τ with noise applied to the reference output weight matrix $\mathbf{W}_\tau^{\text{out}}$ at each time, which are expressed as

$$\hat{\mathbf{y}}_\tau = \mathbf{W}_\tau^\top \hat{\mathbf{x}}_\tau, \quad (16)$$

where $\text{vec}(\mathbf{W}_\tau) \sim \mathcal{N}(\text{vec}(\mathbf{W}_\tau^{\text{out}}), \tilde{\Sigma} \otimes \mathbf{P}_t)$, which is justified by Proposition IV.2. Applying noise to inputs enables approximate computation of optimal inputs through the relationship with free energy. Additionally, applying noise to the output weight matrix provides control input perturbations according to identification accuracy at each time, resulting in automatic adjustment of exploration and exploitation by the controller.

For the input sequence to be determined, $U_t = (\mathbf{u}_t, \dots, \mathbf{u}_{t+H-1}) \in \mathbb{R}^{M \times H}$, perturbed input sequence $V_t = (\mathbf{v}_t, \dots, \mathbf{v}_{t+H-1}) \in \mathbb{R}^{M \times H}$, and output weight matrix sequence $W_t = (\mathbf{W}_t, \dots, \mathbf{W}_{t+H}) \in \mathbb{R}^{\hat{N} \times L \times (H+1)}$, the joint probability density function p_{U_t} of V_t and W_t is expressed as

$$p_{U_t}(V_t, W_t) = p(V_t|U_t, \Sigma)p(W_t|\mathbf{W}_t^{\text{out}}, \mathbf{P}_t, \tilde{\Sigma}), \quad (17)$$

$$p(V_t|U_t, \Sigma) = \prod_{\tau=t}^{t+H-1} \mathcal{N}(\mathbf{v}_\tau|\mathbf{u}_\tau, \Sigma), \quad (18)$$

$$p(W_t|\mathbf{W}_t^{\text{out}}, \mathbf{P}_t, \tilde{\Sigma}) = \prod_{\tau=t}^{t+H} \mathcal{N}(\text{vec}(\mathbf{W}_\tau)|\text{vec}(\mathbf{W}_t^{\text{out}}), \tilde{\Sigma} \otimes \mathbf{P}_t). \quad (19)$$

In UMPPI, the system dynamics are approximated by the ESN model, and at each time t , we seek the input sequence that minimizes the cost function in (3) in the sense of the expected value for p_{U_t} :

$$\underset{U_t \in \mathcal{U}}{\text{minimize}} \mathbb{E}_{p_{U_t}} [\hat{J}_{\text{ctrl}}(V_t, W_t)], \quad (20)$$

$$\begin{aligned} \hat{J}_{\text{ctrl}}(V_t, W_t) &:= S(V_t, W_t; \hat{\mathbf{x}}_t) \\ &+ \sum_{\tau=t}^{t+H-1} \frac{1}{2} (\mathbf{u}_\tau - \mathbf{u}^{\text{ref}})^\top R (\mathbf{u}_\tau - \mathbf{u}^{\text{ref}}), \end{aligned} \quad (21)$$

$$S(V_t, W_t; \hat{\mathbf{x}}_t) := C \left(\mathbf{W}_t^\top \hat{\mathbf{x}}_t, \mathbf{W}_{t+1}^\top \hat{\mathbf{F}}(\hat{\mathbf{x}}_t, \mathbf{v}_t), \dots \right). \quad (22)$$

2) *Free energy relaxation:* This subsection introduces a variational relaxation of the stochastic optimization in (20) using the concept of free energy, leading to an alternative minimization problem in (31). We define the free energy \mathcal{F} as follows:

$$\begin{aligned} \mathcal{F}(S, q, \hat{\mathbf{x}}_t, \lambda) \\ := -\lambda \left\{ \log \left(\mathbb{E}_q \left[\exp \left(-\frac{1}{\lambda} S(V_t, W_t; \hat{\mathbf{x}}_t) \right) \right] \right) \right\}, \end{aligned} \quad (23)$$

where q is a joint probability density function for V_t and W_t which is called the reference density function:

$$q(V_t, W_t) := q(V_t)q(W_t), \quad (24)$$

$$q(V_t) := \prod_{\tau=t}^{t+H-1} \mathcal{N}(\mathbf{v}_\tau | \mathbf{u}^{\text{ref}}, \Sigma), \quad (25)$$

$$q(W_t) := \prod_{\tau=t}^{t+H} \mathcal{N}(\text{vec}(\mathbf{W}_\tau) | \text{vec}(\mathbf{W}_t^{\text{out}}), \tilde{\Sigma} \otimes \mathbf{P}_t). \quad (26)$$

Here, \mathbf{u}^{ref} is the reference input defined in (4). The following two propositions show the relationship between (23) and (20).

Proposition IV.4. For any $U_t \in \mathcal{U}$, the free energy (23) achieves a lower bound of the cost function (20):

$$\mathcal{F}(S, q, \hat{\mathbf{x}}_t, \lambda) \leq \mathbb{E}_{p_{U_t}} [\hat{J}_{\text{ctrl}}(V_t, W_t)]. \quad (27)$$

Proposition IV.5. Suppose that V_t and W_t in (18) and (19) follow the distributions given by

$$p^*(V_t, W_t) := \frac{1}{\eta} \exp \left(-\frac{1}{\lambda} S(V_t, W_t; \hat{\mathbf{x}}_t) \right) q(V_t, W_t), \quad (28)$$

$$\eta := \mathbb{E}_q \left[\exp \left(-\frac{1}{\lambda} S(V_t, W_t; \hat{\mathbf{x}}_t) \right) \right]. \quad (29)$$

Then, equality holds for (27):

$$\mathcal{F}(S, q, \hat{\mathbf{x}}_t, \lambda) = \mathbb{E}_{p^*} [\hat{J}_{\text{ctrl}}(V_t, W_t)]. \quad (30)$$

From Propositions IV.4 and IV.5, designing the distributions of V_t and W_t to satisfy (28) guarantees the optimality of the resulting control input sequence U_t . Thus, we aim to find control inputs to achieve the distribution that minimizes the following Kullback-Leibler divergence:

$$U_t^* = \underset{U_t \in \mathcal{U}}{\text{argmin}} \left\{ \mathbb{E}_{p^*} \left[\log \frac{p^*(V_t, W_t)}{p_{U_t}(V_t, W_t)} \right] \right\}. \quad (31)$$

3) *Sampling-based optimization:* The following proposition provides a computational method for calculating the input (31). This is achieved using importance sampling based on some initial estimate of the input sequence $\hat{U}_t = (\hat{\mathbf{u}}_t, \dots, \hat{\mathbf{u}}_{t+H-1}) \in \mathbb{R}^{M \times H}$.

Proposition IV.6. Suppose that the admissible control input set is given by $\mathcal{U} = \mathbb{R}^{M \times H}$. Then, given any input sequence \hat{U}_t , the control input satisfying (31) is computed as

$$\mathbf{u}_\tau^* = \frac{1}{\tilde{\eta}} \mathbb{E}_{p_{\hat{U}_t}} [w_t(V_t, W_t) \mathbf{v}_\tau], \quad (32)$$

$$w_t(V_t, W_t) := \exp \left(-\frac{1}{\lambda} \left(S(V_t, W_t; \hat{\mathbf{x}}_t) + \sum_{\tau=t}^{t+H-1} (\hat{\mathbf{u}}_\tau - \mathbf{u}^{\text{ref}})^\top R(\mathbf{v}_\tau - \mathbf{u}^{\text{ref}}) \right) \right), \quad (33)$$

$$\tilde{\eta} := \mathbb{E}_{p_{\hat{U}_t}} [w_t(V_t, W_t)], \quad (34)$$

where $p_{\hat{U}_t}$ represents the following distribution:

$$p_{\hat{U}_t}(V_t, W_t) := p(V_t | \hat{U}_t, \Sigma) p(W_t | \mathbf{W}_t^{\text{out}}, \mathbf{P}_t, \tilde{\Sigma}), \quad (35)$$

$$p(V_t | \hat{U}_t, \Sigma) := \prod_{\tau=t}^{t+H-1} \mathcal{N}(\mathbf{v}_\tau | \hat{\mathbf{u}}_\tau, \Sigma). \quad (36)$$

Algorithm 3: MPPI/UMPPPI

Given: Sample size of input/output perturbation K, \tilde{K} , prediction horizon H , initial estimate of input sequence $\hat{U}_t = \hat{U}_{t-1}^*$, reservoir state \mathbf{x}_t , output weight $\mathbf{W}_t^{\text{out}}$, precision matrix \mathbf{P}_t , cost function ℓ , ϕ , inverse temperature λ , and noise covariances $\Sigma, \tilde{\Sigma}$.

$S_{k,\tilde{k}} \leftarrow 0$, $k \in \{0, \dots, K-1\}$, $\tilde{k} \in \{0, \dots, \tilde{K}-1\}$
 Sample $E = \{(\epsilon_t^k, \dots, \epsilon_{t+H-1}^k) \mid \epsilon_\tau^k \sim \mathcal{N}(0, \Sigma), k \in \{0, \dots, \tilde{K}-1\}, \tau \in \{t, \dots, t+H\}\}$

Sample $W = \{(\mathbf{W}_t^{\tilde{k}}, \dots, \mathbf{W}_{t+H}^{\tilde{k}}) \mid \text{vec}(\mathbf{W}_\tau^{\tilde{k}}) \sim \mathcal{N}(\text{vec}(\mathbf{W}_t^{\text{out}}), \tilde{\Sigma} \otimes \mathbf{P}_t), \tilde{k} \in \{0, \dots, \tilde{K}-1\}, \tau \in \{t, \dots, t+H\}\}$

for $k \leftarrow 0$ **to** $K-1$ **do**

$\hat{\mathbf{x}}_t^k \leftarrow \mathbf{x}_t$

for $\tau \leftarrow t$ **to** $t+H-1$ **do**

$\mathbf{v}_\tau^k \leftarrow \hat{\mathbf{u}}_\tau + \epsilon_\tau^k$

$\hat{\mathbf{x}}_{\tau+1}^k \leftarrow \hat{\mathbf{F}}(\hat{\mathbf{x}}_\tau^k, \mathbf{v}_\tau^k)$

for $\tilde{k} \leftarrow 0$ **to** $\tilde{K}-1$ **do**

$S_{k,\tilde{k}} += \ell(\mathbf{W}_\tau^{\tilde{k} \top} \hat{\mathbf{x}}_\tau^k) + \lambda(\hat{\mathbf{u}}_\tau - \mathbf{u}^{\text{ref}})^\top \Sigma^{-1}(\mathbf{v}_\tau^k - \mathbf{u}^{\text{ref}})$

end

end

for $\tilde{k} \leftarrow 0$ **to** $\tilde{K}-1$ **do**

$S_{k,\tilde{k}} += \phi(\mathbf{W}_H^{\tilde{k} \top} \hat{\mathbf{x}}_H^k)$

end

end

$\tilde{\eta} \leftarrow \sum_{k=0}^{K-1} \sum_{\tilde{k}=0}^{\tilde{K}-1} \exp(-\lambda^{-1} S_{k,\tilde{k}})$

$\hat{U}_t^* \leftarrow \hat{U}_t +$

$\tilde{\eta}^{-1} \sum_{k=0}^{K-1} \left[\sum_{\tilde{k}=0}^{\tilde{K}-1} \exp(-\lambda^{-1} S_{k,\tilde{k}}) (\epsilon_t^k, \dots, \epsilon_{t+H-1}^k) \right]$

return \hat{U}_t^*

The resulting UMPPPI algorithm is presented in Algorithm 3. In this algorithm, the expectation in (32) is approximated by Monte Carlo integration using K samples of input noise and \tilde{K} samples of output weight matrices, yielding an approximate optimal input sequence \hat{U}_t^* . To improve sampling efficiency, we use the input sequence from the previous control cycle, $\hat{U}_t = \hat{U}_{t-1}^*$, as the initial estimate of the input sequence \hat{U}_t . Since the input and output noise are independent random variables, Monte Carlo sampling can be efficiently executed in parallel by pre-generating batches of samples.

Remark IV.7. Although Proposition IV.6 is derived under the assumption that the admissible input set \mathcal{U} is unbounded, the algorithm remains practically applicable when \mathcal{U} is bounded. In that case, the updated input sequence can be projected onto \mathcal{U} after each update step. For a detailed discussion of this strategy, see Section III-D2 in Ref. [27].

C. Computational Complexity

We analyze the computational complexity of Algorithm 1. The per-step costs are expressed in terms of the reservoir

state dimension \hat{N} , output dimension L , input dimension M , prediction horizon H , number of input samples K , and number of output weight perturbations \tilde{K} .

To perform matrix-vector products, the RLS update of the output weight matrix $\mathbf{W}_t^{\text{out}} \in \mathbb{R}^{\hat{N} \times L}$ and precision matrix $\mathbf{P}_t \in \mathbb{R}^{\hat{N} \times \hat{N}}$ requires $O(\hat{N}^2 + L\hat{N})$ operations. Sampling K Gaussian input noise sequences costs $O(KHM)$. Drawing \tilde{K} perturbed copies of $\mathbf{W}_t^{\text{out}}$ using a Cholesky factorization of \mathbf{P}_t requires $O(\hat{N}^3 + \tilde{K}L\hat{N}^2)$, where the first term represents the computational cost for preprocessing and the second term represents the computational cost for sampling. For each trajectory and each prediction step, the ESN performs one reservoir state matrix-vector product, one input matrix-vector product, and \tilde{K} output matrix-vector products, requiring $O(\hat{N}^2 + M\hat{N} + \tilde{K}L\hat{N})$ operations per step. The total trajectory simulation cost is $O(KH(\hat{N}^2 + M\hat{N} + \tilde{K}L\hat{N}))$. If the output cost is in quadratic form, evaluating stage and terminal costs $S_{k,\tilde{k}}$ for all (k, \tilde{k}) samples results in $O(KH(M^2 + \tilde{K}L^2))$. Computing weights $\exp(-S_{k,\tilde{k}}/\lambda)$, normalizing factor $\tilde{\eta}$, and forming the weighted average requires $O(K\tilde{K} + KHM)$. Hence, the overall complexity per control step C_{total} is evaluated as follows:

$$\begin{aligned} C_{\text{total}} &= O(\hat{N}^2 + L\hat{N}) + O(KHM) \\ &\quad + O(\hat{N}^3 + \tilde{K}L\hat{N}^2) \\ &\quad + O(KH(\hat{N}^2 + M\hat{N} + \tilde{K}L\hat{N})) \\ &\quad + O(KH(M^2 + \tilde{K}L^2)) + O(K\tilde{K} + KHM) \\ &= O(KH(\hat{N}^2 + M\hat{N} + \tilde{K}L\hat{N} + M^2 + \tilde{K}L^2) \\ &\quad + \hat{N}^3 + \tilde{K}L\hat{N}^2). \end{aligned} \quad (37)$$

Remark IV.8. Focusing on the computational cost of propagating the dynamics over the prediction horizon while simultaneously evaluating uncertainty, the RPPI framework offers a clear advantage over probabilistic MPPI variants that propagate uncertainty through the state vector. Probabilistic MPPI frameworks that represent uncertainty in the state vector must propagate one copy of the state for every uncertainty sample. With state dimension \hat{N} , input dimension M , and output dimension L , a single forward step of the model requires complexity $O(\hat{N}^2 + M\hat{N} + L\hat{N})$. Sampling $K \times \tilde{K}$ trajectories over a horizon of H therefore costs $O(K\tilde{K}H(\hat{N}^2 + M\hat{N} + L\hat{N}))$. In the proposed UMPPI scheme, the hidden state is shared across all weight samples; only the output map is re-evaluated. Therefore, computing $K \times \tilde{K}$ samples requires computational complexity $O(KH(\hat{N}^2 + M\hat{N} + \tilde{K}L\hat{N}))$. For practical settings with $M, L \ll \hat{N}$, the dominant computational terms are $O(K\tilde{K}H\hat{N}^2)$ for the former approach and $O(KH\hat{N}^2 + K\tilde{K}H\hat{N})$ for the latter approach. Therefore, as $\hat{N}, H, K, \tilde{K} \rightarrow \infty$, the sum of the orders of the UMPPI is smaller than that of the probabilistic MPPI that represent uncertainty in the state vector.

V. NUMERICAL EXPERIMENTS

We validate the proposed methods on two benchmark tasks: position control of a Duffing oscillator and water-level regulation of a four-tank system. For each task, we compare three methods for computing the control input in Algorithm 1:

- 1) QMPC [23]: the input is obtained by minimizing the cost in (4). Because the ESN is nonlinear, the model is linearized via a first-order Taylor expansion at every control cycle to yield a QP formulation.
- 2) MPPI: the input is computed by Algorithm 3 with $\tilde{K} = 1$ and $\tilde{\Sigma} = 0$.
- 3) UMPPI: the input is computed by Algorithm 3 with $\tilde{K} \geq 1$ and $\tilde{\Sigma} > 0$.

The hyperparameters are determined through preliminary experiments prior to the execution of Algorithm 1. To verify the concept of simultaneous online identification and control, different plant parameters are used during hyperparameter search and the main experiment. The ESN hyperparameters, namely the sparseness and spectral radius of \mathbf{W}^{res} , the leak rate α , and the range of the input weight matrix \mathbf{W}^{in} , are determined through random search to minimize the cost function (8) when random input signals are applied. Furthermore, the MPPI hyperparameter, the inverse temperature λ , is determined through random search to minimize the cost function (4) when Algorithm 1 is executed using the ESN model with the optimal hyperparameters.

All numerical computations in this study were performed on a host machine running Windows 11 (CPU: Intel Core i9-13900@2.00 GHz, 24 cores; memory: 64 GB) under WSL2 (Ubuntu 22.04). The numerical computation code was implemented in Julia 1.10. In QMPC, QP problems were formulated using the JuMP package [36] and solved with the OSQP package [37]. In RPPI and URPI, 16-thread parallelization on the CPU was employed to perform parallel sampling of the input sequences. All source code and data needed to reproduce the results are publicly available at <https://github.com/ToyotaCRDL/rppi>.

A. Duffing Oscillator

We conduct numerical experiments on a Duffing oscillator [38]. The goal is to control the nonlinear oscillator with cubic stiffness to a reference position using force inputs. This control system is formulated as

$$\begin{aligned} \dot{z}_1(s) &= z_2(s), \\ \dot{z}_2(s) &= -\frac{k}{m}z_1(s) - \frac{c}{m}z_2(s) - \frac{k_{\text{nl}}}{m}z_1^3(s) + \frac{1}{m}\mathbf{u}(s), \\ \mathbf{y}(s) &= z_1(s), \end{aligned} \quad (38)$$

where $s[s]$ is time, $[z_1 \ z_2]^\top [m, m/s]$ are the position and velocity of the oscillator, $\mathbf{u}[N]$ is the external force, and $\mathbf{y} = z_1[m]$ is the position of the oscillator. Additionally, $m[\text{kg}]$ is the mass, $k[N/m]$ is the linear stiffness coefficient, $k_{\text{nl}}[N/m^3]$ is the nonlinear stiffness coefficient, and $c[Ns/m]$ is the damping coefficient. For such a system, we compute control inputs $\mathbf{u}(s) = \mathbf{u}_t$, ($s \in [t\Delta s, (t+1)\Delta s)$, $t = 0, 1, \dots$) while observing output signals $\mathbf{y}_t = \mathbf{y}(t\Delta s)$ ($t = 0, 1, \dots$) at each control period $\Delta s[s]$. The cost function for determining the control input $U_t = (\mathbf{u}_t, \dots, \mathbf{u}_{t+H-1})$ is defined as follows:

$$\begin{aligned} J_{\text{ctrl}}(U_t) &= \sum_{\tau=t}^{t+H-1} \left(\frac{1}{2}Q(\mathbf{y}_\tau - \mathbf{y}^{\text{ref}})^2 + \frac{1}{2}R\mathbf{u}_\tau^2 \right) \\ &\quad + \frac{1}{2}Q(\mathbf{y}_{t+H} - \mathbf{y}^{\text{ref}})^2, \end{aligned} \quad (39)$$

where $\mathbf{y}^{\text{ref}} [\text{m}]$ represents the target position of the oscillator, and $Q > 0 [\text{m}^{-2}]$ and $R > 0 [\text{N}^{-2}]$ are the weight parameters.

The experimental parameters for the Duffing oscillator system are specified below. During hyperparameter tuning, the Duffing oscillator was configured with linear stiffness $k = 1.0$, nonlinear stiffness $k_{\text{nl}} = 1.0$, mass $m = 1.0$, and damping $c = 1.0$. For the main experiments these values were changed to $k = 1.1$, $k_{\text{nl}} = 0.9$, $m = 1.1$, and $c = 0.9$. The control period was fixed at $\Delta s = 0.1$, and (38) was integrated with an explicit Euler scheme using this time step. Cost function weighting employs $Q = 100$ for output tracking and $R = 1$ for input regulation. The reference trajectory alternates between positions $\mathbf{y}^{\text{ref}} = 1.0$ and $\mathbf{y}^{\text{ref}} = -1.0$ every 20 seconds. Control inputs are constrained to the admissible set $\mathcal{U} = [-10, 10]^{1 \times H}$. The ESN parameters are configured as follows. The state matrix uses a dimension of $\hat{N} = 400$ with sparsity factor $\rho = 0.48$ (ratio of non-zero connections) and spectral radius of 0.89. Input weights \mathbf{W}^{in} are set to uniform random values in the range $[-2.0, 2.0]$. The network employs a leak rate of $\alpha = 0.59$ and the hyperbolic tangent activation function $f(x) = \tanh(x)$. For RLS implementation, output weights $\mathbf{W}_{-1}^{\text{out}}$ are initialized as uniform random values in $[-0.1, 0.1]$, the precision matrix is set to $\mathbf{P}_{-1} = \mathbf{I}_{\hat{N}}$, and the discount factor is $\gamma = 1.0$. The control parameters are specified as follows. MPPI operates with the input sample size $K = 1000$, prediction horizon $H = 10$, inverse temperature $\lambda = 1.9$, and noise covariance $\Sigma = 1.9$. UMPPI extends these parameters with the output sample size $\hat{K} = 10$ and output weight covariance $\hat{\Sigma} = 1.0$.

Figure 2 presents the time evolution of system variables under each control method. Figure 2a displays the output response \mathbf{y}_t , while Fig. 2b shows the corresponding control input \mathbf{u}_t . Given the stochastic nature of ESN initialization, MPPI sampling, and UMPPI perturbations, experimental results exhibit inherent variability across executions. Consequently, experiments were conducted across 20 random seeds; for each seed, we independently resampled (i) the ESN state matrix and input-weight matrix, (ii) the initial output-weight matrix, (iii) the MPPI input-perturbation sequences, and (iv) the UMPPI output-weight perturbation sequences. Ensemble means are shown as solid lines, and standard deviations are depicted as shaded regions. The results demonstrate that while QPMPC fails to achieve asymptotic convergence to the reference trajectory, both MPPI and UMPPI successfully attain asymptotic tracking performance. Moreover, QPMPC exhibits substantially higher variability in both control signals and system outputs compared to the reduced variability observed with MPPI and UMPPI.

Figure 3 presents the distribution of time-integrated control costs across multiple random seeds, specifically measured as

$$\sum_{\tau=0}^T \left(\frac{1}{2} Q (\mathbf{y}_{\tau} - \mathbf{y}^{\text{ref}})^2 + \frac{1}{2} R \mathbf{u}_{\tau}^2 \right), \quad (40)$$

where T is the terminal time step, here $T = 400$. Both MPPI and UMPPI achieve substantial reductions in control cost compared to QPMPC, with UMPPI achieving the lowest average cost among the three. Specifically, UMPPI reduces

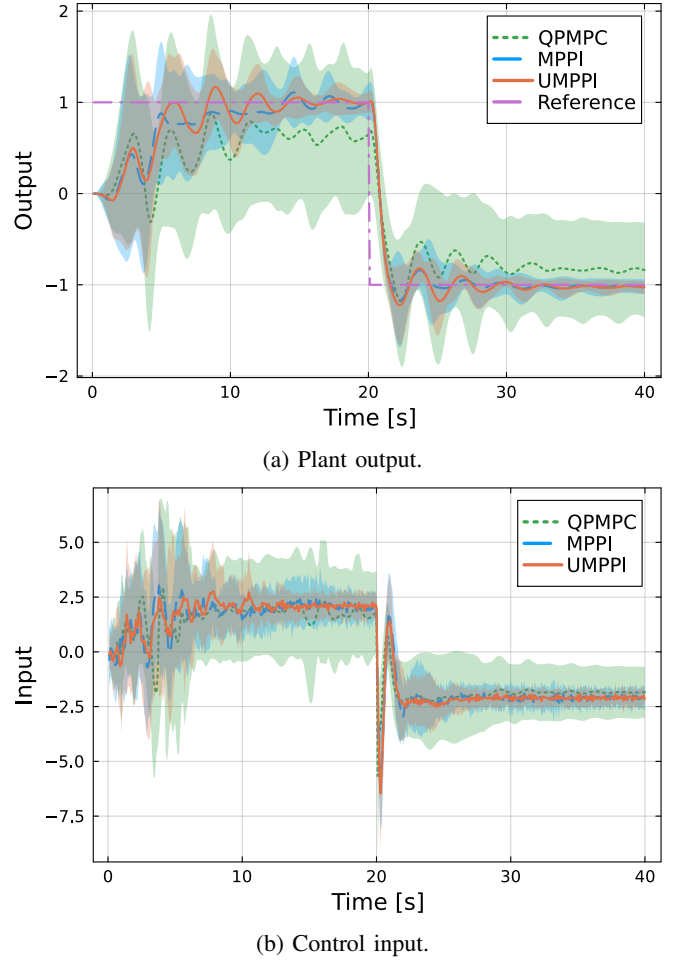


Fig. 2: Time response of the Duffing oscillator. (a): Time response of the controlled output; (b): Time response of the control input. The green dotted line represents QPMPC, the blue dashed line represents MPPI, and the orange solid line represents UMPPI. In (a), the purple dash-dotted line represents the reference output. The shaded areas indicate the standard deviation over multiple random-seed runs.

control cost by approximately 63% compared to QPMPC and by 7% compared to MPPI. In terms of computation time, MPPI requires 0.034 seconds on average to compute control inputs, while UMPPI requires 0.046 seconds. Considering both control cost and computation time, UMPPI provides improved control performance over MPPI at the expense of only a modest increase in computation time.

Figure 4 shows the continuous wavelet scalograms of the control inputs generated by each method. The analysis is confined to the first 6 seconds of each input signal, with the frequency content at each step visualized. Both MPPI and UMPPI exhibit frequency components distributed over a considerably wider range than QPMPC, which is advantageous for capturing the dynamics of the system being identified. This occurs because MPPI, as a random-sampling-based control, inherently produces input signals containing a broad spectrum of frequencies. Moreover, around the area of $t < 3$ s, the UMPPI input signal displays an even wider spread of

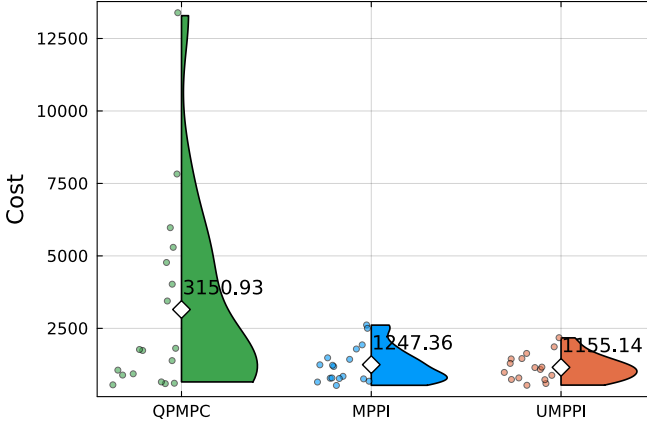


Fig. 3: Comparison of the time-integrated control cost in a Duffing oscillator. The plot is presented in a raincloud style, combining a violin plot (right) to show distribution density and a scatter plot (left) to display individual data points. Diamond markers and numerical values indicate the mean of each distribution.

frequency components compared to MPPI. UMPPI achieves this by injecting perturbations into the control input based on the identification accuracy of its output weight matrix. This behavior suggests an intrinsic mechanism within UMPPI that automatically balances exploration and exploitation.

B. Four-Tank System

We conduct numerical experiments on a four-tank system [39]. The goal is to regulate the water levels in the lower two tanks to their reference values by adjusting the pump flow rates. This control system is formulated as

$$\begin{aligned}
 \dot{z}_1(s) &= -\frac{a_1}{A_1} \sqrt{2gz_1(s)} + \frac{a_3}{A_1} \sqrt{2gz_3(s)} + \frac{b_1}{A_1} u_1(s), \\
 \dot{z}_2(s) &= -\frac{a_2}{A_2} \sqrt{2gz_2(s)} + \frac{a_4}{A_2} \sqrt{2gz_4(s)} + \frac{b_2}{A_2} u_2(s), \\
 \dot{z}_3(s) &= -\frac{a_3}{A_3} \sqrt{2gz_3(s)} + \frac{(1-b_2)}{A_3} u_2(s), \\
 \dot{z}_4(s) &= -\frac{a_4}{A_4} \sqrt{2gz_4(s)} + \frac{(1-b_1)}{A_4} u_1(s), \\
 \mathbf{y}(s) &= [z_1(s) \ z_2(s)]^\top,
 \end{aligned} \tag{41}$$

where z_i [cm] ($i = 1, \dots, 4$) are the water levels in the four tanks and $\mathbf{u} = [u_1 \ u_2]^\top$ [cm³/s, cm³/s] are the volumetric flow rates delivered by the two pumps. For $i = 1, \dots, 4$, A_i [cm²] are the cross-sectional areas of the tanks and a_i [cm²] are the outlet areas; for $i = 1, 2$, the dimensionless parameters $b_i \in (0, 1)$ specify the flow split between upper and lower tanks. The constant g [cm/s²] denotes gravitational acceleration. The cost function to determine the control input

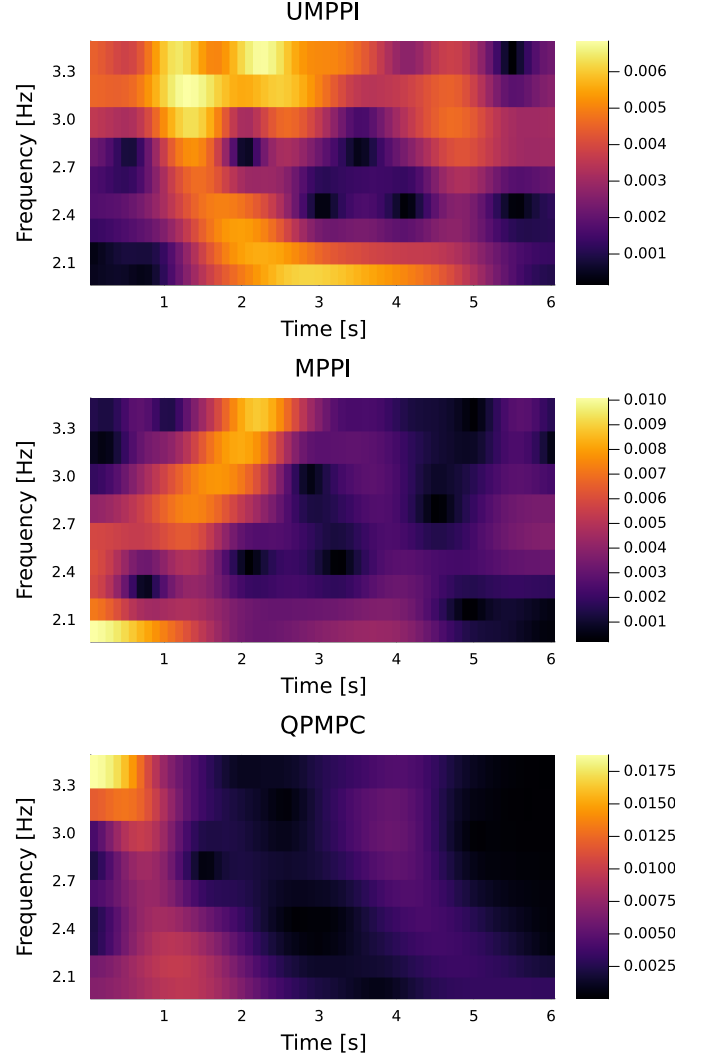


Fig. 4: Averaged continuous-wavelet scalogram of the control signals for the Duffing oscillator. Each signal is analyzed with a complex Morlet wavelet (frequency-domain variance 2π). The horizontal axis shows time, the vertical axis shows frequency, and color indicates the coefficient magnitude. From top to bottom: results for UMPPI, MPPI, and QPMPC.

$U_t = (\mathbf{u}_t, \dots, \mathbf{u}_{t+H-1})$ is defined as follows:

$$\begin{aligned}
 J_{\text{ctrl}}(U_t) &= \sum_{\tau=t}^{t+H-1} \left(\frac{1}{2} (\mathbf{y}_\tau - \mathbf{y}^{\text{ref}})^\top Q (\mathbf{y}_\tau - \mathbf{y}^{\text{ref}}) \right. \\
 &\quad \left. + \frac{1}{2} (\mathbf{u}_\tau - \mathbf{u}^{\text{ref}})^\top R (\mathbf{u}_\tau - \mathbf{u}^{\text{ref}}) \right) \\
 &\quad + \frac{1}{2} (\mathbf{y}_{t+H} - \mathbf{y}^{\text{ref}})^\top Q (\mathbf{y}_{t+H} - \mathbf{y}^{\text{ref}}),
 \end{aligned} \tag{42}$$

where \mathbf{y}^{ref} [cm, cm] denotes the reference water levels, \mathbf{u}^{ref} [cm³/s, cm³/s] the reference flow rates, and $Q, R \in \mathbb{R}^{2 \times 2}$ are positive-definite weighting matrices (the entries of Q have units cm⁻², whereas those of R have units s²cm⁻⁶).

Experimental parameters for the four-tank system are listed below. System configuration: tank cross-sectional areas $A_1 = A_3 = 28$, $A_2 = A_4 = 32$; outlet areas $a_1 = a_3 = 0.071$,

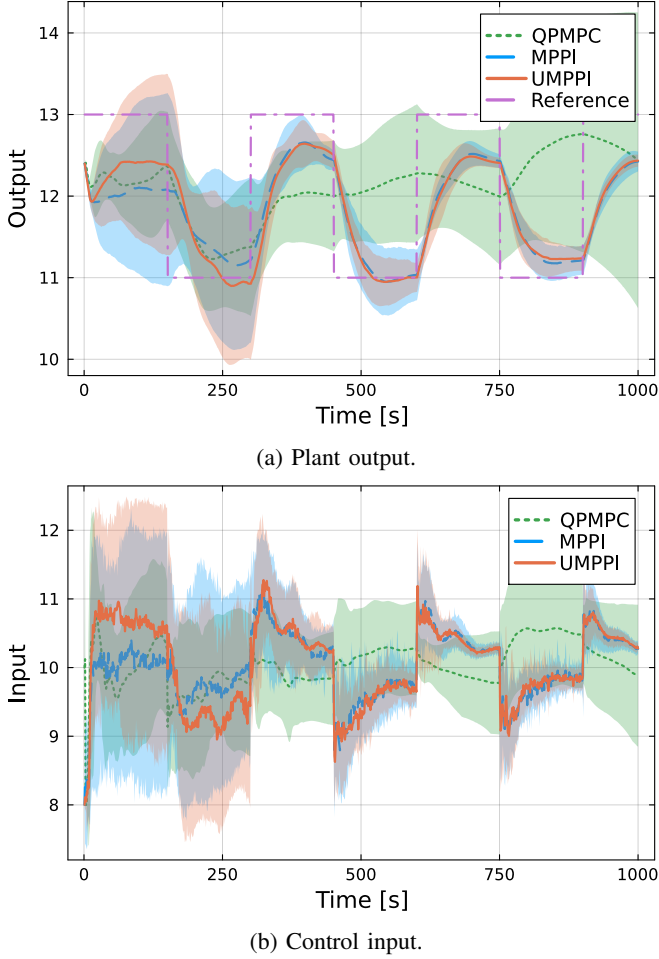


Fig. 5: Time response of the four-tank system. (a): Time response of the first component of the controlled output in the two-dimensional system; (b): Time response of the first component of the control input. The green dotted line represents QPMPC, the blue dashed line represents MPPI, and the orange solid line represents UMPPI. In (a), the purple dash-dotted line represents the reference output. The shaded areas show the standard deviation over multiple random-seed runs.

$a_2 = a_4 = 0.057$; volume-distribution factors were set to $b_1 = 0.7$, $b_2 = 0.6$ during hyperparameter tuning and changed to $b_1 = 0.693$, $b_2 = 0.606$ in the main experiments; sampling period $\Delta s = 1.0$; cost weights $Q = I_2$, $R = I_2$; reference levels alternating between $\mathbf{y}^{\text{ref}} = [13 \ 13]^\top$ and $\mathbf{y}^{\text{ref}} = [11 \ 11]^\top$ every 150 s. ESN configuration: state dimension $\hat{N} = 400$; reservoir sparsity factor $\rho = 0.17$; spectral radius 0.78; input weights uniformly distributed in $[-1.5, 1.5]$; leak rate $\alpha = 0.078$; activation function $\tanh(x)$. RLS initialization: output weights $\mathbf{W}_{-1}^{\text{out}}$ uniformly distributed in $[-0.1, 0.1]$; precision matrix $\mathbf{P}_{-1} = I_{\hat{N}}$; discount factor $\gamma = 1.0$. MPPI configuration: reference input $\mathbf{u}^{\text{ref}} = [10 \ 10]^\top$; input constraints $\mathcal{U} = [8, 12]^{2 \times H}$; sample size $K = 1000$; horizon $H = 10$; inverse temperature $\lambda = 0.71$; noise covariance $\Sigma = 0.71I_2$. UMPPI configuration: output sample size $\tilde{K} = 10$; covariance matrix $\tilde{\Sigma} = 0.1I_2$.

The time responses of each variable when controlled by

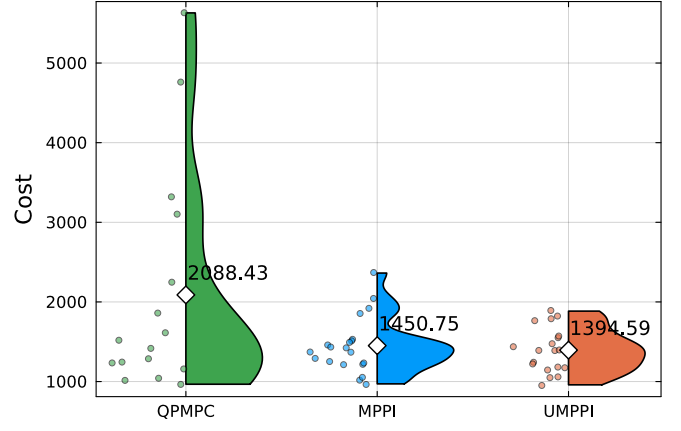


Fig. 6: Comparison of the time-integrated control cost in a four-tank system. The plot is presented in a raincloud style, combining a violin plot (right) to show distribution density and a scatter plot (left) to display individual data points. Diamond markers and numerical values indicate the mean of each distribution.

each method are shown in Fig. 5. Figure 5a shows the time response of the first component of the output \mathbf{y}_t , and Fig. 5b shows the time response of the first component of the input \mathbf{u}_t . While the plant output under QPMPC gradually deviates from the reference trajectory, both MPPI and UMPPI successfully track the reference whenever it changes. MPPI and UMPPI can achieve smaller input-output variability compared to QPMPC.

The results of computing and visualizing the time-integrated control cost over multiple random seeds, namely

$$\sum_{\tau=0}^T \left(\frac{1}{2} (\mathbf{y}_\tau - \mathbf{y}^{\text{ref}})^\top Q (\mathbf{y}_\tau - \mathbf{y}^{\text{ref}}) + \frac{1}{2} (\mathbf{u}_\tau - \mathbf{u}^{\text{ref}})^\top R (\mathbf{u}_\tau - \mathbf{u}^{\text{ref}}) \right), \quad (43)$$

are shown in Fig. 6. Here, the terminal time step T is set to $T = 1000$. Both MPPI and UMPPI achieve substantial reductions in control cost compared to QPMPC, with UMPPI achieving the best overall performance. Specifically, UMPPI reduces control cost by 33.1% compared to QPMPC, and by 3.9% relative to MPPI. In terms of computation time, MPPI requires 0.037 seconds on average to compute control inputs, while UMPPI requires 0.049 seconds. Overall, UMPPI provides improved control performance over MPPI with only a small additional computational cost.

Figure 7 presents the averaged continuous wavelet scalograms of control inputs for UMPPI, MPPI, and QPMPC. We focus on the first 60 seconds of each trial, with the magnitude of the coefficients visualized at every step. Both MPPI and UMPPI exhibit broader frequency distributions than QPMPC, and, around $t = 40$ s, UMPPI displays the widest spread. These results confirm that MPPI's random-sampling approach introduces diverse spectral content, and UMPPI's perturbations further enhance automatic exploration-exploitation balancing.

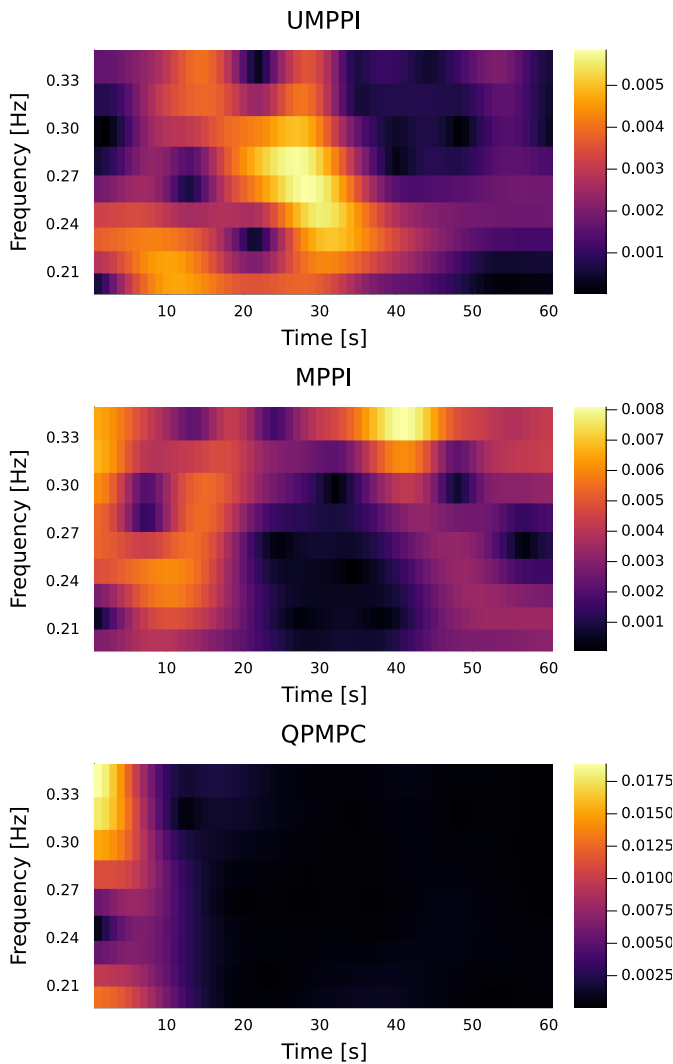


Fig. 7: Averaged continuous-wavelet scalogram of the control signals for the four-tank system. Each signal is analyzed with a complex Morlet wavelet (frequency-domain variance 2π). The horizontal axis shows time, the vertical axis shows frequency, and color indicates the coefficient magnitude. From top to bottom: results for UMPPI, MPPI, and QPMPC.

VI. CONCLUSION

We presented a control framework that integrates echo state networks (ESN) with model predictive path integral control (MPPI). Our proposed methods, RPPI and URPI, combine rapid ESN learning with sampling-based MPPI without linearization to achieve online control for nonlinear systems. In URPI, the exploration-exploitation mechanism generates broader frequency content, improving identification accuracy. Through numerical experiments on the Duffing oscillator and four-tank systems, we demonstrated that URPI achieves 30–60% lower control costs than conventional quadratic programming methods. Overall, the proposed framework offers a systematic solution for the simultaneous identification and control of nonlinear systems. Future work should address theoretical analysis and pursue hardware validation in robotics,

aerospace, and process control applications.

ACKNOWLEDGMENTS

The authors thank Dr. Hiroaki Yoshida and Ms. Shihori Koyama of Toyota Central R&D Labs., Inc., and Mr. Takumu Fujioka of Nagoya Institute of Technology, for their helpful discussions and suggestions. Generative-AI tools were used to assist with manuscript proofreading and to prototype simulation scripts.

REFERENCES

- [1] L. Ljung, *System Identification (2nd Ed.): Theory for the User*. USA: Prentice Hall PTR, 1999.
- [2] F. L. Lewis, D. Vrabie, and V. L. Syrmos, *Optimal Control*. John Wiley & Sons, 2012.
- [3] H. Nijmeijer and A. Van der Schaft, *Nonlinear Dynamical Control Systems*. Springer, 1990, vol. 175.
- [4] Y. Pan and J. Wang, “Nonlinear Model Predictive Control Using a Recurrent Neural Network,” in *2008 IEEE International Joint Conference on Neural Networks (IEEE World Congress on Computational Intelligence)*, Jun. 2008, pp. 2296–2301.
- [5] Y. Chen, Y. Shi, and B. Zhang, “Optimal Control Via Neural Networks: A Convex Approach,” in *International Conference on Learning Representations*, Sep. 2018.
- [6] Z. Yan and J. Wang, “Model Predictive Control of Nonlinear Systems With Unmodeled Dynamics Based on Feedforward and Recurrent Neural Networks,” *IEEE Transactions on Industrial Informatics*, vol. 8, no. 4, pp. 746–756, Jan. 2012.
- [7] F. Bonassi, C. F. O. da Silva, and R. Scattolini, “Nonlinear MPC for Offset-Free Tracking of systems learned by GRU Neural Networks,” *IFAC-PapersOnLine*, vol. 54, no. 14, pp. 54–59, Jan. 2021.
- [8] E. Terzi, F. Bonassi, M. Farina, and R. Scattolini, “Learning Model Predictive Control with Long Short-Term Memory Networks,” *International Journal of Robust and Nonlinear Control*, vol. 31, no. 18, pp. 8877–8896, 2021.
- [9] G. Cao, E. M.-K. Lai, and F. Alam, “Gaussian Process Model Predictive Control of Unknown Non-linear Systems,” *IET Control Theory & Applications*, vol. 11, no. 5, pp. 703–713, Mar. 2017.
- [10] P. Polcz, T. Péni, and R. Tóth, “Efficient Implementation of Gaussian Process-based Predictive Control by Quadratic Programming,” *IET Control Theory & Applications*, vol. 17, no. 8, pp. 968–984, 2023.
- [11] T. Salzmann, E. Kaufmann, J. Arrizabalaga, M. Pavone, D. Scaramuzza, and M. Ryll, “Real-Time Neural MPC: Deep Learning Model Predictive Control for Quadrotors and Agile Robotic Platforms,” *IEEE Robotics and Automation Letters*, vol. 8, no. 4, pp. 2397–2404, Apr. 2023.
- [12] C. K. Williams and C. E. Rasmussen, *Gaussian Processes for Machine Learning*. MIT press Cambridge, MA, 2006, vol. 2.
- [13] J. Park and J. Choi, “Gaussian Process Online Learning With a Sparse Data Stream,” *IEEE Robotics and Automation Letters*, vol. 5, no. 4, pp. 5977–5984, Oct. 2020.
- [14] A. Alessio and A. Bemporad, “A Survey on Explicit Model Predictive Control,” in *Nonlinear Model Predictive Control: Towards New Challenging Applications*, ser. Lecture Notes in Control and Information Sciences. Berlin, Heidelberg: Springer, 2009, pp. 345–369.
- [15] M. Kvasnica, J. Hledík, I. Rauová, and M. Fikar, “Complexity Reduction of Explicit Model Predictive Control via Separation,” *Automatica*, vol. 49, no. 6, pp. 1776–1781, Jun. 2013.
- [16] S. Chen, K. Saulnier, N. Atanasov, D. D. Lee, V. Kumar, G. J. Pappas, and M. Morari, “Approximating Explicit Model Predictive Control Using Constrained Neural Networks,” in *2018 Annual American Control Conference (ACC)*, Jun. 2018, pp. 1520–1527.
- [17] U. Forssell and L. Ljung, “Closed-Loop Identification Revisited,” *Automatica*, vol. 35, no. 7, pp. 1215–1241, Jul. 1999.
- [18] S. J. Qin, “An Overview of Subspace Identification,” *Computers & Chemical Engineering*, vol. 30, no. 10, pp. 1502–1513, Sep. 2006.
- [19] H. Jaeger, “Adaptive Nonlinear System Identification with Echo State Networks,” in *Advances in Neural Information Processing Systems*, vol. 15. MIT Press, 2002.
- [20] H. Jaeger, M. Lukoševičius, D. Popovici, and U. Siewert, “Optimization and Applications of Echo State Networks with Leaky-Integrator Neurons,” *Neural Networks*, vol. 20, no. 3, pp. 335–352, Apr. 2007.

- [21] M. Salmen and P. G. Ploger, "Echo State Networks used for Motor Control," in *Proceedings of the 2005 IEEE International Conference on Robotics and Automation*, Apr. 2005, pp. 1953–1958.
- [22] C. Sun, M. Song, D. Cai, B. Zhang, S. Hong, and H. Li, "A Systematic Review of Echo State Networks From Design to Application," *IEEE Transactions on Artificial Intelligence*, vol. 5, no. 1, pp. 23–37, Jan. 2024.
- [23] Y. Pan and J. Wang, "Model Predictive Control of Unknown Nonlinear Dynamical Systems Based on Recurrent Neural Networks," *IEEE Transactions on Industrial Electronics*, vol. 59, no. 8, pp. 3089–3101, Aug. 2012.
- [24] J. P. Jordanou, E. A. Antonelo, and E. Camponogara, "Echo State Networks for Practical Nonlinear Model Predictive Control of Unknown Dynamic Systems," *IEEE Transactions on Neural Networks and Learning Systems*, vol. 33, no. 6, pp. 2615–2629, Jun. 2022.
- [25] B. B. Schwedersky, R. C. C. Flesch, and S. B. Rovea, "Adaptive Practical Nonlinear Model Predictive Control for Echo State Network Models," *IEEE Transactions on Neural Networks and Learning Systems*, vol. 33, no. 6, pp. 2605–2614, Jun. 2022.
- [26] B. B. Schwedersky, R. C. C. Flesch, and S. B. Rovea, "Echo State Networks for Online, Multi-step MPC Relevant Identification," *Engineering Applications of Artificial Intelligence*, vol. 108, p. 104596, Feb. 2022.
- [27] G. Williams, P. Drews, B. Goldfain, J. M. Reh, and E. A. Theodorou, "Information-Theoretic Model Predictive Control: Theory and Applications to Autonomous Driving," *IEEE Transactions on Robotics*, vol. 34, no. 6, pp. 1603–1622, Feb. 2018.
- [28] G. Williams, A. Aldrich, and E. Theodorou, "Model Predictive Path Integral Control using Covariance Variable Importance Sampling," *arXiv:1509.01149 [cs]*, Oct. 2015.
- [29] M. Kazim, J. Hong, M.-G. Kim, and K.-K. Kim, "Recent Advances in Path Integral Control for Trajectory Optimization: An Overview in Theoretical and Algorithmic Perspectives," *Annual Reviews in Control*, vol. 57, p. 100931, Jan. 2024.
- [30] A. Sanchez-Gonzalez, N. Heess, J. T. Springenberg, J. Merel, M. Riedmiller, R. Hadsell, and P. Battaglia, "Graph Networks as Learnable Physics Engines for Inference and Control," in *Proceedings of the 35th International Conference on Machine Learning*. PMLR, Jul. 2018, pp. 4470–4479.
- [31] J. Park, M. R. Babaei, S. A. Munoz, A. N. Venkat, and J. D. Hedengren, "Simultaneous Multistep Transformer Architecture for Model Predictive Control," *Computers & Chemical Engineering*, vol. 178, p. 108396, Oct. 2023.
- [32] W. Wang, H. Zhang, Y. Wang, Y. Tian, and Z. Wu, "Fast Explicit Machine Learning-Based Model Predictive Control of Nonlinear Processes Using Input Convex Neural Networks," *Industrial & Engineering Chemistry Research*, vol. 63, no. 40, pp. 17 279–17 293, Oct. 2024.
- [33] G. Williams, B. Goldfain, P. Drews, K. Saigol, J. M. Reh, and E. A. Theodorou, "Robust Sampling Based Model Predictive Control with Sparse Objective Information," in *Robotics: Science and Systems*, vol. 14, 2018, p. 2018.
- [34] J. Yin, Z. Zhang, and P. Tsiotras, "Risk-Aware Model Predictive Path Integral Control Using Conditional Value-at-Risk," in *2023 IEEE International Conference on Robotics and Automation (ICRA)*, May 2023, pp. 7937–7943.
- [35] B. Farhang-Boroujeny, *Adaptive Filters: Theory and Applications*. John Wiley & sons, 2013.
- [36] M. Lubin, O. Dowson, J. Dias Garcia, J. Huchette, B. Legat, and J. P. Vielma, "JuMP 1.0: Recent Improvements to a Modeling Language for Mathematical Optimization," *Mathematical Programming Computation*, 2023.
- [37] B. Stellato, G. Banjac, P. Goulart, A. Bemporad, and S. Boyd, "OSQP: An Operator Splitting Solver for Quadratic Programs," *Mathematical Programming Computation*, vol. 12, no. 4, pp. 637–672, 2020.
- [38] A. Marconato, J. Sjöberg, J. Suykens, and J. Schoukens, "Identification of the Silverbox Benchmark Using Nonlinear State-Space Models," *IFAC Proceedings Volumes*, vol. 45, no. 16, pp. 632–637, Jul. 2012.
- [39] K. Johansson, "The Quadruple-Tank Process: A Multivariable Laboratory Process with an Adjustable Zero," *IEEE Transactions on Control Systems Technology*, vol. 8, no. 3, pp. 456–465, May 2000.
- [40] I. S. Gradshteyn and I. M. Ryzhik, *Table of Integrals, Series, and Products*. Academic press, 2014.

APPENDIX

We provide proofs for Propositions IV.2–IV.6. The results of Proposition IV.2 is obtained by extending the analysis in

Ref. [35] to the case of ESNs, where the estimated parameters take a matrix form. The proofs of Propositions IV.4–IV.6 extend the derivation of the MPPI presented in Ref. [27]. Specifically, Proposition IV.4 parallels Eq. (13) in Ref. [27]; Proposition IV.5 derives along the same route in Section III-A of that work; and Proposition IV.6 corresponds to Eq. (27) of the same reference.

Proof of Proposition IV.2 From the optimality condition $\partial J_{\text{id}}(\mathbf{W}_t^{\text{out}*})/\partial \mathbf{W}_t^{\text{out}*} = 0$, we obtain

$$\mathbf{W}_t^{\text{out}*} = \mathbf{A}_t^{-1} \mathbf{B}_t. \quad (44)$$

where $\mathbf{B}_t := \sum_{\tau=0}^t \gamma^{t-\tau} \mathbf{x}_\tau \mathbf{y}_\tau^\top$. From (11) and (44),

$$\begin{aligned} \mathbf{W}_t^{\text{out}*} - \bar{\mathbf{W}}^{\text{out}} &= \mathbf{P}_t (\mathbf{B}_t - \mathbf{A}_t \bar{\mathbf{W}}^{\text{out}}) \\ &= \mathbf{P}_t \sum_{\tau=0}^t \gamma^{t-\tau} \mathbf{x}_\tau \epsilon_\tau^\top. \end{aligned} \quad (45)$$

Therefore,

$$\text{vec}(\mathbf{W}_t^{\text{out}*} - \bar{\mathbf{W}}^{\text{out}}) = \begin{bmatrix} \mathbf{P}_t \sum_{\tau=0}^t \gamma^{t-\tau} \mathbf{x}_\tau \epsilon_{\tau,1} \\ \vdots \\ \mathbf{P}_t \sum_{\tau=0}^t \gamma^{t-\tau} \mathbf{x}_\tau \epsilon_{\tau,L} \end{bmatrix}, \quad (46)$$

where $\epsilon_{\tau,\ell}$ is the ℓ -th component of ϵ_τ . Using the fact that

$$\mathbb{E}[\epsilon_{k,\ell} \epsilon_{\tilde{k},\tilde{\ell}}] = \begin{cases} \sigma_k^2 & k = \tilde{k}, \ell = \tilde{\ell}, \\ 0 & \text{otherwise,} \end{cases} \quad (47)$$

we obtain

$$\begin{aligned} &\mathbb{E}[\text{vec}(\mathbf{W}_t^{\text{out}*} - \bar{\mathbf{W}}^{\text{out}}) \text{vec}(\mathbf{W}_t^{\text{out}*} - \bar{\mathbf{W}}^{\text{out}})^\top] \\ &= \begin{bmatrix} \sigma_1^2 \mathbf{P}_t & 0 & \cdots & 0 \\ 0 & \sigma_2^2 \mathbf{P}_t & & \vdots \\ \vdots & & \ddots & 0 \\ 0 & \cdots & 0 & \sigma_L^2 \mathbf{P}_t \end{bmatrix} \\ &= \tilde{\Sigma} \otimes \mathbf{P}_t, \end{aligned} \quad (48)$$

where we assumed $\gamma = 1$. This completes the proof. \square

Proof of Proposition IV.4 By using Jensen's inequality [40], the free energy $\mathcal{F}(S, q, \hat{\mathbf{x}}_t, \lambda)$ is bounded as

$$\begin{aligned} \mathcal{F}(S, q, \hat{\mathbf{x}}_t, \lambda) & \\ &\leq \mathbb{E}_{p_{U_t}} \left[S(V_t, W_t; \hat{\mathbf{x}}_t) + \lambda \log \frac{p_{U_t}(V_t, W_t)}{q(V_t, W_t)} \right]. \end{aligned} \quad (49)$$

For the second term, by taking the reference probability density function q as (25) and (26), it follows

$$\begin{aligned} &\mathbb{E}_{p_{U_t}} \left[\log \frac{p_{U_t}(V_t, W_t)}{q(V_t, W_t)} \right] \\ &= \mathbb{E}_{p_{U_t}} \left[\log \frac{p(V_t | U_t, \Sigma)}{q(V_t)} \right] \\ &= \frac{1}{2} \sum_{\tau=t}^{t+H-1} (\mathbf{u}_\tau - \mathbf{u}^{\text{ref}})^\top \Sigma^{-1} (\mathbf{u}_\tau - \mathbf{u}^{\text{ref}}). \end{aligned} \quad (50)$$

Substituting (50) into (49) completes the proof. \square

Proof of Proposition IV.5 In (49), taking the probability density function of V_t and W_t as (28), we obtain

$$\begin{aligned} & \mathbb{E}_{p^*} \left[\hat{J}_{\text{ctrl}}(V_t, W_t) \right] \\ &= \mathbb{E}_{p^*} \left[S(V_t, W_t; \hat{\mathbf{x}}_t) + \lambda \log \frac{p^*(V_t, W_t)}{q(V_t, W_t)} \right], \end{aligned} \quad (51)$$

For the second term on the right-hand side,

$$\begin{aligned} & \mathbb{E}_{p^*} \left[\log \frac{p^*(V_t, W_t)}{q(V_t, W_t)} \right] \\ &= \mathbb{E}_{p^*} \left[\log \left(\frac{1}{\eta} \exp \left(-\frac{1}{\lambda} S(V_t, W_t; \hat{\mathbf{x}}_t) \right) \right) \right] \\ &= -\frac{1}{\lambda} \mathbb{E}_{p^*} [S(V_t, W_t; \hat{\mathbf{x}}_t)] - \log(\eta). \end{aligned} \quad (52)$$

By substituting (52) into (51),

$$\mathbb{E}_{p^*} [\hat{J}_{\text{ctrl}}(V_t, W_t)] = -\lambda \log(\eta) = \mathcal{F}(S, q, \hat{\mathbf{x}}_t, \lambda). \quad (53)$$

This completes the proof. \square

Proof of Proposition IV.6 First, we show that the optimal input satisfies $\mathbf{u}_\tau^* = \mathbb{E}_{p^*}[\mathbf{v}_\tau]$. This is shown as follows:

$$\begin{aligned} U_t^* &= \underset{U_t \in \mathcal{U}}{\operatorname{argmin}} \left\{ \mathbb{E}_{p^*} \left[\log \left(\frac{p^*(V_t, W_t)}{p_{U_t}(V_t, W_t)} \right) \right] \right\} \\ &= \underset{U_t \in \mathcal{U}}{\operatorname{argmax}} \{ \mathbb{E}_{p^*} [\log(p(V_t|U_t, \Sigma))] \} \\ &= \underset{U_t \in \mathcal{U}}{\operatorname{argmin}} \left\{ \mathbb{E}_{p^*} \left[\sum_{\tau=0}^{H-1} (\mathbf{v}_\tau - \mathbf{u}_\tau)^\top \Sigma^{-1} (\mathbf{v}_\tau - \mathbf{u}_\tau) \right] \right\}. \end{aligned} \quad (54)$$

In the third line, $p(V_t|U_t, \Sigma)$ defined in (18) was substituted. When $\mathcal{U} = \mathbb{R}^{M \times H}$, the solution to this optimization problem satisfies $\mathbf{u}_\tau^* = \mathbb{E}_{p^*}[\mathbf{v}_\tau]$, ($\tau = t, \dots, t+H-1$).

Next, by introducing importance sampling using \hat{U}_t , we show (32). The above optimal input is expressed as

$$\begin{aligned} \mathbb{E}_{p^*}[\mathbf{v}_\tau] &= \int \int \mathbf{v}_\tau p^*(V_t, W_t) dV_t dW_t \\ &= \int \int \mathbf{v}_\tau \frac{p^*(V_t, W_t)}{p_{\hat{U}_t}(V_t, W_t)} p_{\hat{U}_t}(V_t, W_t) dV_t dW_t \\ &= \mathbb{E}_{p_{\hat{U}_t}} [w'_t(V_t, W_t) \mathbf{v}_\tau], \end{aligned} \quad (55)$$

where

$$w'_t(V_t, W_t) := \frac{p^*(V_t, W_t)}{p_{\hat{U}_t}(V_t, W_t)}. \quad (56)$$

By the definition of p^* and $p_{\hat{U}_t}$ in (28) and (35),

$$w'_t(V_t, W_t) = \frac{\frac{1}{\eta} \exp \left(-\frac{1}{\lambda} S(V_t, W_t; \hat{\mathbf{x}}_t) \right) q(V_t)}{p(V_t|\hat{U}_t, \Sigma)}. \quad (57)$$

Using the reference density function $q(V_t)$ in (25), we have

$$\begin{aligned} \frac{q(V_t)}{p(V_t|\hat{U}_t, \Sigma)} &= \frac{\prod_{\tau=t}^{t+H-1} \mathcal{N}(\mathbf{v}_\tau | \mathbf{u}^{\text{ref}}, \Sigma)}{\prod_{\tau=t}^{t+H-1} \mathcal{N}(\mathbf{v}_\tau | \hat{\mathbf{u}}_\tau, \Sigma)} \\ &= \exp \left(-\sum_{\tau=t}^{t+H-1} (\hat{\mathbf{u}}_\tau - \mathbf{u}^{\text{ref}})^\top \Sigma^{-1} (\mathbf{v}_\tau - \mathbf{u}^{\text{ref}}) \right) \\ &\quad \cdot \exp \left(\frac{1}{2} \sum_{\tau=t}^{t+H-1} (\hat{\mathbf{u}}_\tau - \mathbf{u}^{\text{ref}})^\top \Sigma^{-1} (\hat{\mathbf{u}}_\tau - \mathbf{u}^{\text{ref}}) \right). \end{aligned} \quad (58)$$

Substituting this into (57), we obtain

$$w'_t(V_t, W_t) = \frac{1}{\eta'} w_t(V_t, W_t), \quad (59)$$

where

$$\eta' := \exp \left(-\frac{1}{2} \sum_{\tau=t}^{t+H-1} (\hat{\mathbf{u}}_\tau - \mathbf{u}^{\text{ref}})^\top \Sigma^{-1} (\hat{\mathbf{u}}_\tau - \mathbf{u}^{\text{ref}}) \right) \eta. \quad (60)$$

Here, η' can be transformed as follows:

$$\begin{aligned} \eta' &= \mathbb{E}_{p^*} [\eta'] \\ &= \mathbb{E}_{p_{\hat{U}_t}} \left[\eta' \frac{p^*(V_t, W_t)}{p(V_t|\hat{U}_t, \Sigma) p(W_t|\mathbf{W}_t^{\text{out}}, \mathbf{P}_t, \tilde{\Sigma})} \right] \\ &= \mathbb{E}_{p_{\hat{U}_t}} [\eta' w'_t(V_t, W_t)] \\ &= \mathbb{E}_{p_{\hat{U}_t}} [w_t(V_t, W_t)] = \tilde{\eta}. \end{aligned} \quad (61)$$

Substituting (59) and (61) into (55) completes the proof. \square